Title

Molecular beam scattering from flat jets of liquid dodecane and water

Permalink

https://escholarship.org/uc/item/2718r2mx

Journal

Natural Sciences, 4(2-3)

ISSN

2698-6248

Authors

Yang, Walt

Foreman, Madison M

Saric, Steven

et al.

Publication Date

2024-06-01

DOI

10.1002/ntls.20240009

Peer reviewed

Molecular Beam Scattering from Flat Jets of Liquid Dodecane and Water

Walt Yang[1,2], Madison M. Foreman[1,2], Steven Saric[1,2], Alec M. Wodtke[3], Kevin R. Wilson[2], Daniel M.

Neumark[1,2,]*

[1] *Department of Chemistry, University of California, Berkeley, CA 94720, USA*

[2] *Chemical Sciences Division, Lawrence Berkeley National Laboratory, Berkeley, CA 94720, USA*

[3] *Department of Dynamics at Surfaces, Max Planck Institute for Multidisciplinary Sciences, am Faßberg 11, 37077 Göttingen, Germany*

[*]**Author to whom correspondence should be addressed: <u>dneumark@berkeley.edu</u>**

ABSTRACT

Molecular beam experiments in which gas molecules are scattered from liquids provide detailed, microscopic perspectives on the gas–liquid interface. Extending these methods to volatile liquids while maintaining the ability to measure product energy and angular distributions presents a significant challenge. The incorporation of flat liquid jets into molecular beam scattering experiments in our laboratory has allowed us to demonstrate their utility in uncovering dynamics in this complex chemical environment. Here, we summarize recent work on the evaporation and scattering of Ne, CD_4, ND_3, and D_2O from a dodecane flat liquid jet and present first results on the evaporation and scattering of Ar from a cold salty water jet. In the evaporation experiments, Maxwell–Boltzmann flux distributions with a $\cos\theta$ angular distribution are observed. Scattering experiments reveal both impulsive scattering and trapping followed by thermal desorption. Super-specular scattering is observed for all four species scattered from dodecane and is attributed to anisotropic momentum transfer to the liquid surface. In the impulsive scattering channel, rotational excitation of the polyatomic scatterers is a significant energy sink, and these species accommodate more readily on the dodecane surface compared to Ne. Our preliminary results on cold salty water jets suggest that Ar atoms undergo vapor-phase collisions when evaporating from the liquid surface. Initial scattering experiments characterize the mechanisms of Ar interacting with an aqueous jet, allowing for comparison to dodecane systems.

Key Points

- Molecular beam scattering from flat liquid jets is a powerful technique to elucidate mechanistic detail at the gas–liquid interface.

- Previous dodecane scattering experiments have uncovered angularly-resolved TD fractions and energy transfer at the interface for several small molecule scatterers.

- Preliminary results on scattering from cold salty water reveal mechanisms of interaction between argon and an aqueous jet.

KEYWORDS

Water interface, flat liquid jets, molecular beam scattering, interfacial dynamics, energy transfer, kinematic modeling

I. INTRODUCTION

The gas–liquid interface is a chemical environment that governs many key processes essential for everyday life. Notable examples include the adsorption of O_2 and the desorption of CO_2 at the air–lung interface,[1,2] controlling air–fuel mixing in internal combustion engines[3] and the treatment of amine gases,[4] and the formation of acid rain and modulation of atmospheric ozone.[5-9] Extracting information on molecular-level structure, kinetics, and dynamics at the gas–liquid interface requires methods specifically geared toward surface studies.[10-12] Novel spectroscopic and kinetics techniques have been developed to address this challenge.[13-15] Deep ultraviolet electronic sum frequency generation spectroscopy has revealed charge-transfer-to-solvent transitions in anions at the air–water interface[16-19] and vibrational spectroscopy has been used to interrogate formic acid orientation with angstrom-level depth resolution.[20] Additionally, thin film and microdroplet studies have uncovered augmented chemical reaction rates compared to their bulk counterparts.[21-24] This paper focuses on molecular beam experiments that probe the gas–liquid interface.

Fundamental interactions between particles in the gas and liquid phases underlie both structural characteristics and dynamical phenomena at the interface. Molecular beam scattering experiments offer an effective means of probing these interactions, building on the knowledge developed through molecular beam scattering from solid surfaces to probe nonreactive[25-28] and reactive[27,29] processes. Enabled by developments of the liquid microjet by Faubel[30-32] and the wetted wheel by Fenn[33] and Siegbahn,[34] Nathanson, Minton, and others have paved the way for molecular beam experiments on the gas–liquid interface.[35-44] These experiments have elucidated an unprecedented level of mechanistic detail behind gas–liquid interactions.[45,46]

The advent of microfluidic chips that generate flat liquid jets[47] led us to perform angle-resolved molecular beam scattering experiments on the vacuum–dodecane interface. In this paper, we highlight

60   our previous results[48-50] scattering select species from a dodecane flat liquid jet, where we compared how

61   the dodecane surface differs from other hydrocarbon surfaces such as squalane.[35,51] We also present new

62   results on the evaporation and scattering of Ar from a cold salty water jet. The experiments performed in

63   our group show how molecular beam scattering coupled with flat liquid jets provides a powerful

64   approach to understanding interfacial behavior.

65   Evaporation and scattering experiments require maintaining a clean liquid surface and, to be

66   compatible with a vacuum environment, the chosen liquids must have a low vapor pressure to minimize

67   the contribution of collisions with the vapor jacket surrounding the surface of the jet. The flat liquid jet

68   satisfies these conditions by introducing a continuously flowing liquid into the vacuum chamber as well

69   as granting access to more volatile solvents than those compatible with the wetted wheel approach (*cf.*

70    $\sim 10^{-2}$ and $< 10^{-3}$ Torr, respectively). Compared to cylindrical jets, a flat jet offers a larger target (~ 1

71   mm versus ~ 30 μm) for molecular beam scattering, leading to substantially higher scattering signal.

72   Additionally, a flat jet has a well-defined surface normal, thereby enabling angularly-resolved

73   measurements.[46]

74   In our prior work on dodecane flat jets ($P_{vap} = 1.5 \times 10^{-2}$ Torr at 275 K), we characterized the liquid

75   interface by measuring the angular and translational energy distributions of Ne, CD_4, ND_3, and D_2O

76   evaporating and scattering from dodecane.[48-50] Through evaporation of these species from the jet, we

77   deduced that conditions were present for nascent scattering to take place. We then considered two

78   limiting nonreactive scattering mechanisms at the gas–liquid interface. Impulsive scattering (IS) arises

79   when incident gas molecules undergo inelastic collisions with the surface, while thermal desorption

80   (TD) takes place when trapping leads to residence times at the surface that are long enough for

81   thermalization.[26,45] Based on previous angularly-resolved measurements, the IS pathway is expected to

82   lead to specular scattering, or detection of scattered particles at angles determined by the initial energy

83   and incident trajectory, whereas TD yields $\cos\theta$ angular distributions with respect to the surface

84   normal.[26,52] Note that while the simple partitioning between IS and TD is a useful framework for

85   interpreting experimental observations, in reality scattering is a much more complicated process.[53]

86   In our prior scattering experiments, we examined the partitioning between these two mechanistic

87   pathways and found that interfacial behavior is largely dictated by scatterer identity. We also measured

88   TD fractions and the degree of energy transfer in the IS channel at multiple deflection angles. Super-

89   specular scattering was observed for all four scatterers. We compared our findings to those of Saecker

90   and Nathanson, where Ne, CH_4, D_2O, and NH_3 were scattered from a squalane ($P_{vap} = 10^{-7}$ Torr at 295

91   K) wetted wheel at a single deflection angle.[51] In that same study, a glycerol surface was also

92   interrogated, and it was found that squalane presents a rougher and softer surface than glycerol, leading

93   to a higher likelihood of trapping scatterers at the interface.

94   More complex and volatile liquids have been studied since, such as surfactant-coated

95   NaBr/glycerol,[41,43] concentrated aqueous LiBr and LiCl solutions,[38,40] and surfactant-coated aqueous LiBr

96   solutions.[54] Studies on these aqueous systems have been crucial in understanding the air–water interface

97   at a fundamental level but are limited by the usage of cylindrical microjets which do not provide angular

98   resolution. Thus, we demonstrate the first angularly-resolved experiments reporting mechanistic detail at

99   the gas–water interface through the evaporation and scattering of Ar from a cold aqueous 8 molal LiBr

100   flat jet ($P_{vap} = 5.2 \times 10^{-2}$ Torr at 225 K). Preliminary results show that evaporation of Ar from the jet can

101   be well-described by a Maxwell–Boltzmann flux distribution. Additionally, TD fractions at select

102   scattering angles suggest that cold salty water is a more accommodating surface than dodecane for rare

103   gases. Given the angular specificity of the flat liquid jet and that the deflection angle can alter

104   mechanistic partitioning so drastically, these first results lay the foundation for investigating angular-

105   dependent reactivity at the water surface.

II. EXPERIMENTAL APPARATUS

All experiments are performed in a crossed molecular beam instrument[55,56] adapted for gas–liquid scattering as described in detail previously.[48] The apparatus comprises three vacuum chambers housing the pulsed molecular beam source, collision region, and rotatable detector, all evacuated by turbomolecular pumps.
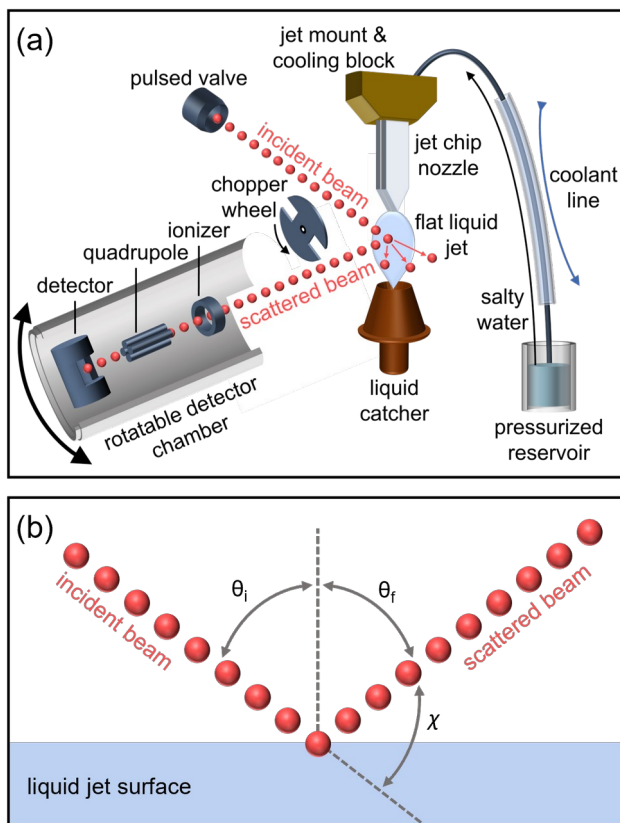
Figure 1. (a) Schematic diagram of the scattering setup for a cold salty water jet. All components are situated inside the collision chamber (not shown). The chopper wheel can be translated perpendicular to the detector axis. (b) Definition of the incidence angle θ_i, scattering angle θ_f, and deflection angle $\chi = 180° - (\theta_i + \theta_f)$.

A schematic diagram of the entire scattering setup is shown in Fig. 1. The pulsed molecular beam is generated within the source chamber and interacts with the flat liquid jet in the collision chamber. A large-area, liquid nitrogen-cooled copper wall within the scattering chamber yields a very high pumping speed for vapor from the jet. Scattered products then enter the triply-differentially pumped rotatable detector chamber that comprises an electron impact ionizer (80 eV electron kinetic energy), quadrupole

121 mass filter, and ion detection assembly. Fig. 1 defines the incidence angle θ_i, scattering angle θ_f, and

122 deflection angle $\chi = 180° - (\theta_i + \theta_f)$. For the dodecane studies, θ_i is chosen to be 45, 60, or 80°, enabled

123 by rotation of the chip holder. Due to geometrical constraints of the scattering apparatus, outgoing

124 angles θ_f are restricted to a range between $90° - \theta_i$ and 90°. For scattering from salty water, θ_i is chosen

125 to be 60°.

126 As in prior work, a piezoelectric valve (MassSpecpecD BV, Enschede)[57,58] generates the pulsed

127 molecular beams used herein. Ne, CD_4, ND_3, and D_2O supersonic beams are seeded in helium at

128 respective compositions of 10, 0.75, 1.5, and ~0.5 %.[49,50] The Ar beam is prepared similarly by seeding

129 ~10 % Ar in He, and stagnation conditions are typically 293 K and 3000 Torr. Note that a dimer ratio of

130 5 % is present for D_2O, but no dimers were detected for either CD_4 or ND_3. The velocities of the

131 molecular beams are characterized by time-of-flight (TOF) measurements with a rotating (200 Hz)

132 chopper wheel (two slits, 14 μs open time). This results in beam velocities of 1562 ± 165, 1732 ± 185,

133 1730 ± 205, 1791 ± 347, and 1454 ± 208 m s^{-1} (FWHM), with mean translational energies of 23.7, 29.3,

134 28.8, 33.4, and 41.5 kJ mol^{-1} for Ne, CD_4, ND_3, D_2O, and Ar, respectively.

135 Within the collision chamber, flat liquid jets are formed using a microfluidic chip.[47] As described

136 previously for the dodecane jet, an HPLC pump is employed to deliver the solvent through a pre-cooling

137 stage to the jet nozzle at a flow rate of 3.5 mL min^{-1} and a flow velocity of 10 m s^{-1}, leading to a detector

138 viewing time of ~600 μs. Typical dimensions of the first flat jet sheet are 1.5×4.5 mm^2 (W × H),

139 measured via calibrated images captured by a high-resolution camera, with a thickness estimated to be

140 ~1.5 μm at its center.[32] For the cold salty water jet, a 2.3 L glass cylinder containing 8 m LiBr dissolved

141 in H_2O (Milli-Q®, MilliporeSigma) is housed in a pressurized stainless steel reservoir. This aqueous

142 solution was chosen due to its relatively low freezing point, suppressing the vapor pressure of water, and

143 extensive studies having been performed on molecular beam scattering from this liquid.[38,40,42,59] To

144 operate the jet at a flow rate of ~2 mL min^{-1} at a temperature of ~226 K at the jet nozzle, the reservoir

145   is pressurized to 85 bar. This leads to a flow velocity of 7 m s^{-1} and a detector viewing time of ~500 μs

146   (~4 mm at the interaction region with the detector gate valve opened to a 2 mm circular aperture).

147   For the dodecane jet, a stainless-steel chip holder is used, and the temperature of the jet is recorded

148   using a thermocouple attached to the holder. The temperature difference $T_{holder} - T_{liq}$ (the true liquid

149   temperature at the interaction region) is estimated to be less than 0.5 °C owing to the high isobaric heat

150   capacity and low vapor pressure of dodecane.[60,61] This results in liquid temperatures T_{liq} of 283, 273, 269,

151   and 274 K for dodecane doped with Ne, CD_4, ND_3, and D_2O, respectively, for the evaporation

152   experiments. $T_{liq} = 269$ K for all dodecane scattering experiments. The temperature gradient across the

153   jet surface is expected to be small due to the high isobaric heat capacity and low vapor pressure of

154   dodecane, suppressing evaporative cooling effects.[60,61] The samples were prepared through a process that

155   has been described previously for Ne, CD_4, ND_3, and D_2O in dodecane (n-$C_{12}H_{26}$, TCI America

156   #D0968).[48-50] For the scattering experiments, pure dodecane is used after vacuum-degassing with pure

157   He.

158   Multiple modifications have been implemented to operate a cold salty water jet. Marine-grade 464

159   brass rather than stainless steel is used for part of the chip holder assembly due to its increased corrosion

160   resistance. To achieve significantly lower jet temperatures, a commercial marine utility pump (Xylem

161   Rule iL280P) circulates an ethanol bath held at 233 K through an in-line stainless-steel counter-current

162   pre-cooling stage that surrounds the solvent delivery line. The salty water flows through this stage for

163   ~1 m prior to entering the collision chamber. For additional cooling, flexible Cu braids are attached to a

164   solid Cu extrusion from the cryogenically cooled Cu wall inside of the collision chamber. These braids

165   connect to the chip holder with temperature T_{holder} recorded by a thermocouple. The temperature

166   difference $T_{holder} - T_{liq}$ is estimated to be less than 3 °C for the salty water jet due to its relatively low

167   vapor pressure.[40,46] For both evaporation and scattering experiments, T_{holder} was measured to be 226 K.

168 The salty water sample is prepared by dissolving Ar in 8 m aqueous LiBr by vacuum-degassing the

169 liquid. For scattering from salty water, 8 m LiBr is used after vacuum-degassing with pure N_2.

170   The translational energy distribution of evaporated and scattered species is determined by time-of-

171 flight (TOF) measurements. In the evaporation experiments, time zero is set by the chopper wheel

172 positioned between the jet and the detector. Detector angles θ_f range from 0 to 90° with respect to the

173 surface normal. In scattering experiments, the chopper wheel is translated away from the detector axis,

174 and the moment when the most intense part of the pulsed molecular beam reaches the interaction region

175 defines time zero at the interaction region. As a result, the temporal resolution of the scattering TOF

176 measurements is limited by the quality of the pulsed beam profiles. For Ne, CD_4, ND_3, D_2O, and Ar, the

177 valve opening time is set to 15, 15, 12, 30, and 13 μs, respectively. Temporal widths measured at the

178 detector were 28, 26, 27, 43, and 40 μs, respectively. The "beam-off" data is subtracted from "beam-on"

179 data to achieve background-subtracted scattering spectra. To ensure that systematic error is limited

180 throughout, angular distributions are measured in a back-and-forth manner as described prior.[48-50]

181 Acquisition times for dodecane are typically between 5 and 10 minutes for a single spectrum, while this

182 is extended to 20 minutes for salty water.

183 **III. RESULTS OF EVAPORATION EXPERIMENTS ON DODECANE**

184   To isolate TD and determine that conditions for nascent scattering exist, evaporation TOF spectra

185 were taken for doped dodecane jets. Ne, CD_4, ND_3, and D_2O evaporation from their respective doped

186 dodecane jets are shown in Fig. 2(a–c) for θ_f = 0, 30, and 60°. Since these solutes are at thermal

187 equilibrium with the liquid surface prior to evaporation, the product flux f can be described by a

188 Maxwell–Boltzmann (MB) flux distribution[62]

189
$$f_{MB}(v) \propto S_0(v,\theta)\, v^3 \exp\left(\frac{-m v^2}{2 R T_{liq}}\right)$$
$$(1)$$

190   where v and m are the velocity and molecular mass of the evaporating molecule and R is the universal

191   gas constant. $S_0(v, \theta)$ is the velocity- and angle-dependent sticking coefficient.

192   At $\theta_f = 0°$, Maxwellian behavior of the evaporating particles is observed; as θ_f approaches $60°$, the

193   TOF profiles for all four species broaden toward longer arrival times. This broadening, or sub-

194   Maxwellian behavior, is from an isotropic background due to molecular desorption from the

195   cryogenically cooled Cu wall that persists even if the jet is moved out of the viewing angle of the

196   detector.[49,50,63] Thus, the TOF spectra are fitted by a linear combination of MB distributions at T_{liq} and

197   T_{bkg}.
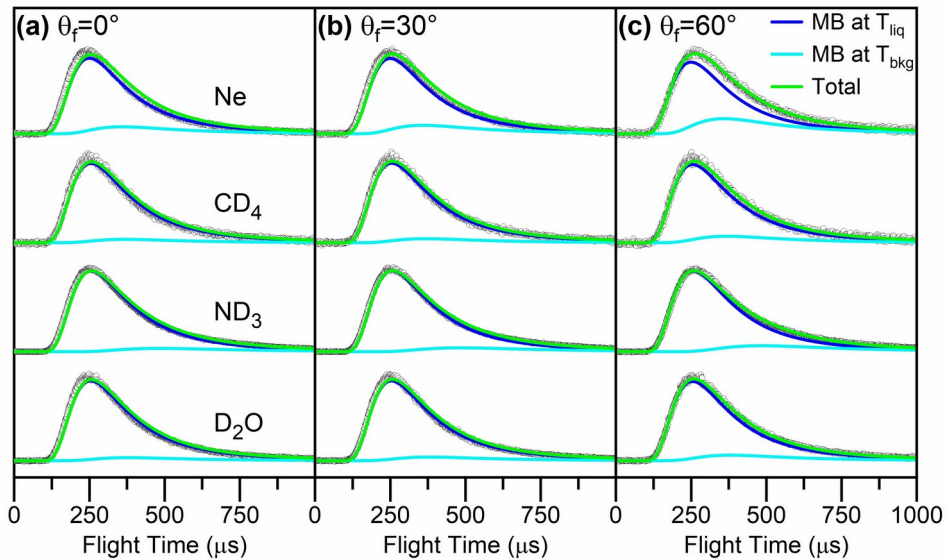
198

199   **Figure 2.** Normalized evaporation TOF spectra of Ne, CD_4, ND_3, and D_2O from doped liquid dodecane
200   flat jets at (a) $\theta_f = 0°$, (b) $\theta_f = 30°$, and (c) $\theta_f = 60°$. TOF distributions are fitted with a combination of
201   Maxwell–Boltzmann velocity distributions at $T_{liq} = 283$, 273, 269, and 274 K (blue traces) and at
202   $T_{bkg} = 137$, 131, 75, and 123 K (light blue traces), respectively. The absolute intensity of the T_{bkg}
203   component is kept constant for all angles. The sum of the two contributions is shown by the green traces.

9
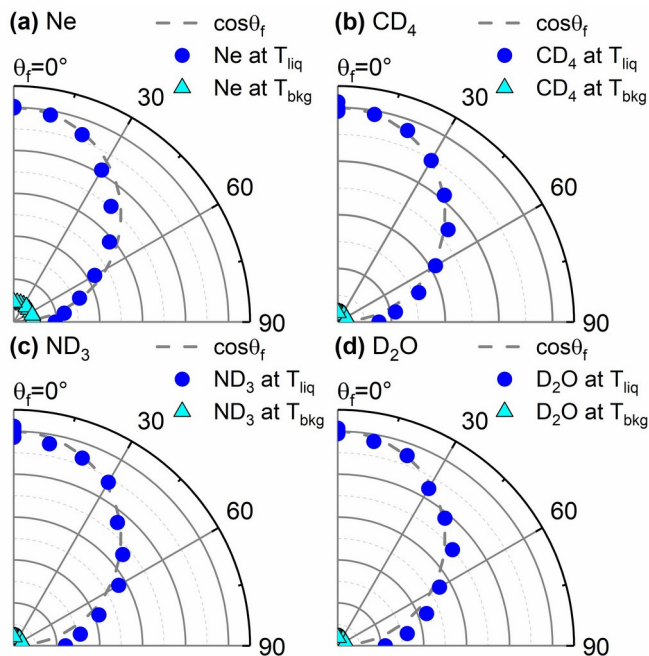
Figure 3. Angular plots created from the integrated, non-normalized intensities of the Maxwell–Boltzmann simulations at T_{liq} and T_{bkg} (blue circles and cyan triangles, respectively) of (a) Ne, (b) CD_4, (c) ND_3, and (d) D_2O evaporation data at various detector angles. The cosine function representing the expected angular distribution for evaporation is indicated by the dashed gray curve.

Integrating the fitted TOF spectra results in angular distributions where the total evaporative flux is plotted as a function of θ_f in Fig. 3 for Ne, CD_4, ND_3, and D_2O. As expected for an evaporative process from a flat surface and provided that detailed balance holds,[62,64] the contributions at T_{liq} follow a $\cos\theta_f$ distribution.[65,66] Given that all four species exhibit both Maxwellian translational energy distributions and $\cos\theta_f$ angular distributions after accounting for background signal, our results indicate that the sticking coefficient $S_0(v, \theta)$ in Eq. 1 can be assumed to be unity[62] and that the evaporating species do not interact measurably with the vapor sheath around the jet. The latter observation implies that vapor sheath interactions will also be insignificant in scattering experiments.

IV. RESULTS OF SCATTERING EXPERIMENTS ON DODECANE

TOF spectra of Ne, CD_4, ND_3, and D_2O scattered from a dodecane jet are shown in Fig. 4(a–c) for $\theta_i = 60°$ and detector angles $\theta_f = 30$, 60, and 80°. Overall, comparing TOF profiles at the same θ_f reveals faster arrival times and narrower TOF distributions for scattered Ne compared to the polyatomic

221 scatterers. The polyatomic scatterers behave similarly with only slight differences in the scattering

222 profiles, though the ND_3 and D_2O distributions extend to longer arrival times compared to CD_4. As

223 θ_f increases, the TOF profiles shift toward earlier arrival times. This trend is also observed for incidence

224 angles of 45 and 80°.

225   The TOF distributions are fitted using two contributions—one assigned to a faster component from IS

226 and the other a slower one from TD. The IS component is fitted to the flux distribution for a supersonic

227 (SS) molecular beam in Eq. 2[67,68]

228
$$f_{SS}(v) \propto v^3 \exp\left(\frac{-m(v-v_{SS})^2}{2RT_{SS}}\right)$$
$$(2)$$

229 with average flow velocity v_{SS} and average temperature T_{SS}. The fits to the TOF spectra with a linear

230 combination of SS and MB distributions representing the two scattering channels are also shown in Fig.

231 4.[45,69] Note that the fitting procedure involves convolution with the full molecular beam temporal

232 profiles.
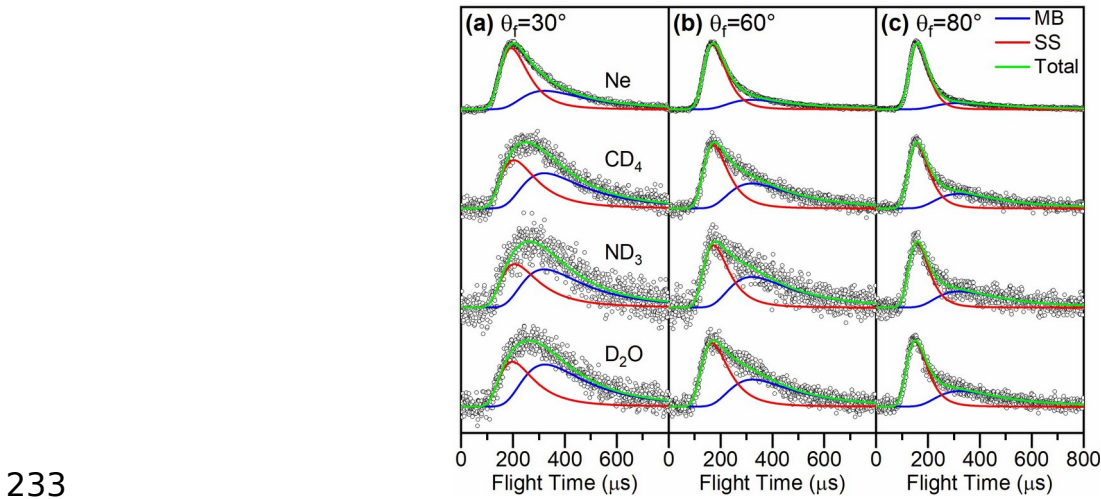
233

234 **Figure 4.** Normalized TOF spectra of Ne, CD_4, ND_3, and D_2O scattering from a dodecane flat jet with
235 $\theta_i = 60°$ at (a) $\theta_f = 30°$, (b) $\theta_f = 60°$, and (c) $\theta_f = 80°$. The data are fitted by the sum (green traces) of an
236 SS distribution (red traces) and an MB distribution (blue traces) at the liquid jet temperature. Mean
237 translational energies E_i for Ne, CD_4, ND_3, and D_2O are 23.7, 29.3, 28.8, and 33.4 kJ mol^{-1}, respectively.

238   For all four species, the TD contribution drops as θ_f increases, resulting in narrower, faster TOF

239   spectra. This result reflects the $\cos\theta_f$ angular distribution for TD, leading to less TD at higher θ_f. From

240   the fitted TOF profiles, the polyatomic scatterers exhibit considerably more TD than Ne, especially at

241   values of θ_f approaching the surface normal. It is also observed that the TD fractions for Ne are smaller

242   than those for the polyatomic scatterers at all deflection angles. The TD fractions for the polyatomic

243   species are similar, but overall, the trend manifests as $ND_3 > D_2O \approx CD_4 > Ne$. This trend is discussed in

244   more detail in Section IVb.

245   Angular distributions from integrating the fitted TOF profiles are shown in Fig. 5(a–d) for the four

246   scatterers at $\theta_i = 60°$. For the TD channel, the integrated intensities closely follow a $\cos\theta_f$ angular

247   distribution, consistent with our evaporation results, indicating that these particles have equilibrated at

248   T_{liq} prior to desorbing. Although one might expect to observe specular scattering in the angular

249   distributions of the IS channel, we observe super-specular scattering for all four systems, where the

250   maximum IS intensity is found at $\theta_f > \theta_i$; for these systems, the angular distribution peaks at $\theta_f = 70°$.

251   This result is attributed to collisions that favor momentum transfer along the surface normal.[70,71]
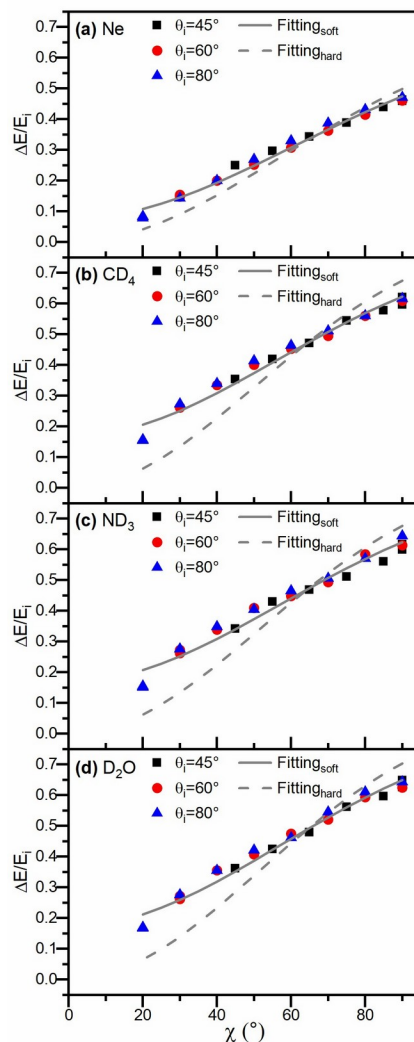

12
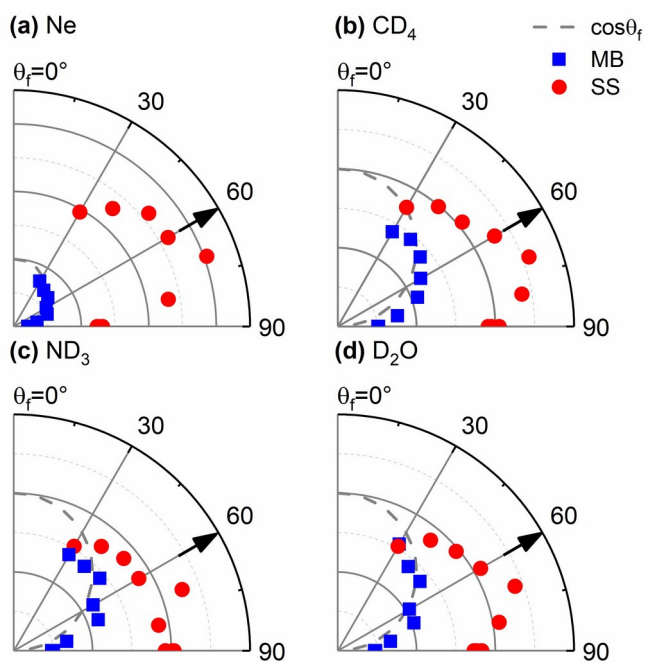
Figure 5. Angular plots created from the integrated, non-normalized intensities of scattering at $\theta_i = 60°$ for (a) Ne, (b) CD_4, and (c) ND_3, and (d) D_2O. Blue squares represent the TD (MB distribution) and red circles the IS (SS distribution) contributions to the TOF fits. The cosine function representing the expected angular distribution for evaporation is indicated by the dashed, gray curve. Arrows indicate the specular angle.

IVa. DISCUSSION OF IMPULSIVE SCATTERING FROM DODECANE

The scattering TOF profiles provide energetic information in the form of changes to the translational energies of the scattered molecular beams. Specifically, analyzing the IS channel within the scattering TOF profiles through established kinematic models reveals key findings on energy transfer at the gas–liquid interface. The soft-sphere kinematic model, previously applied to other scattering studies,[72,73] describes the average fractional energy loss as a function of deflection angle. The model is given by Eq. 3: [72,74,75]

$$\left(\frac{\Delta E}{E_i}\right) \approx \frac{2\mu}{(1+\mu)^2} ¿$$

$$¿$$

where the absolute change in translational energy is $\Delta E = E_i - \langle E_{IS} \rangle$, with incident translational energy E_i and average energy in the IS channel $\langle E_{IS} \rangle$. The mass ratio $\mu = m_{gas}/m_{eff}$ between the gas molecule and the effective surface mass, the total internal excitation of both the scatterer and surface E_{int}, the liquid temperature T_{liq}, and the well depth of the gas–surface interaction potential V are also included. The scattering geometry is represented by the deflection angle $\chi = 180° - (\theta_i + \theta_f)$. In essence, this is a modified line-of-centers model where internal excitation is allowed. The V/E_i and $-2RT_{liq}/E_i$ terms account for the effects of the interaction potential and thermal surface motions on $\Delta E/E_i$, respectively.[75] In prior studies, similar models have related microscopic quantities like collisional energy transfer to macroscopic properties such as bulk densities.[51,76]

Figure 6. Average fractional energy loss as a function of deflection angle for impulsively scattered (a) Ne, (b) CD_4, (c) ND_3, and (d) D_2O from a dodecane flat jet. Incident translational energies are 23.7, 29.3, 28.8, and 33.4 kJ mol^{-1}, respectively. The solid curves give predictions for the soft-sphere model, where the incident particle interacts with a localized region of the surface with an effective mass, m_{eff}, and this region may increase its internal energy, E_{int}, during collisions. The dashed curves give predictions for the hard-sphere model where internal excitation has been set to zero. The fitting results for Ne, CD_4, ND_3, and D_2O with the soft-sphere model are m_{eff} = 61, 52, 55, and 54 amu and E_{int} = 2.1, 5.3, 5.1, and 5.8 kJ mol^{-1}, respectively, whereas the hard-sphere model predicts m_{eff} = 48, 34, 36, and 35 amu, respectively.

Fig. 6(a–d) shows the measured fractional translational energy loss plotted against deflection angle for scattering of Ne, CD_4, ND_3, and D_2O. The fractional energy loss increases with χ regardless of incidence angle for all four scatterers, consistent with observations made prior in the literature for other liquid surfaces.[35,72] For Ne, the fractional energy loss ranges from 0.15 to 0.46 between χ = 30° and 90°. For the polyatomic scatterers, D_2O energy loss increases from 0.27 to 0.64, while CD_4 and ND_3 behave

14

290 similarly, with values ranging from 0.27 to 0.61 for both species. This trend of larger fractional energy

291 losses for the polyatomic species compared to Ne at all values of χ is also present for the other two

292 incidence angles chosen in this study.

293 The results of fitting the soft-sphere kinematic model to the fractional energy loss values are also

294 shown in Fig. 6 alongside the hard-sphere model fits, where E_{int} is set to be zero. Note that this model

295 assumes the scatterer and surface to be individual spheres, whereas molecular dynamics simulations find

296 the structure of the dodecane–vacuum interface to be much more complex.[77] The free-fit parameters are

297 m_{eff} and E_{int} where applicable, and V is set to a fixed value given by the well depths of the Lennard-Jones

298 potential[78-81] between the scatterers and dodecane. For both kinematic models, values of V for Ne, CD_4,

299 ND_3, and D_2O are 0.9, 1.9, 2.8, and 3.6 kJ mol^{-1}, respectively. If V is also set to be zero, assuming a

300 completely noninteracting system, the best-fitted curves do not change to a significant degree. Inspecting

301 the best-fit curves for the two models, the fractional energy loss behavior in the IS channel is best

302 described by the soft-sphere kinematic model for all four scatterers. Due to the small value for E_{int} in the

303 case of Ne, the hard-sphere and soft-sphere fits are more similar to one another compared to the fits for

304 the polyatomic scatterers.

305 Comparing these fractional energy loss values to literature values from squalane experiments at a fixed

306 deflection angle of $\chi = 90°$,[51] we observe that the relative behavior between the four scatterers is similar

307 for dodecane and squalane. The energy loss ordering for scattering from dodecane is Ne < CD_4 < ND_3 <

308 D_2O, which agrees with the reported ordering of Ne < CH_4 < NH_3 < D_2O for scattering from squalane.

309 These values can be found in Table 1.

310 At $\chi = 45$ and $90°$, we observe fractional energy loss values of 0.25 and 0.46, respectively, for Ne

311 scattered from dodecane. In a comparable study performed on a squalane surface,[35] fractional energy

312 loss values of 0.36 and 0.58 were reported. Given that the incident beam energies were similar (*cf.*

313 23.7 kJ mol^{-1} in this work, 32 kJ mol^{-1} in ref. [35]), it is plausible that more internal modes within the

15

314   squalane surface contribute to collision events compared to the dodecane surface, leading to the

315   reduction in fractional energy loss. Thus, we conclude that squalane is a "softer," less rigid surface than

316   dodecane. Further discussion on the relative rigidity between these two surfaces can be found in Section

317   IVb.

318   The best-fit soft sphere curves result in recovered values for m_{eff} and E_{int} in the scattering of Ne, CD_4,

319   ND_3, and D_2O, shown in Table 1. Given that the molecular mass of dodecane is ∼170 amu, these results

320   suggest that only four CH_2/CH_3 groups within any dodecane molecule contributes to fractional energy

321   loss in the IS channel, as the effective surface masses are about one-third of the dodecane mass. The

322   polyatomic scatterers all exhibit similar values of E_{int}, contrasting with the smaller value for Ne

323   scattering.

324   Examining the fitted values for the total internal excitation and considering that all four species have

325   nearly identical masses and initial energies, the larger values for E_{int} that arise from molecular scattering

326   compared to Ne scattering are likely due to the presence of internal degrees of freedom. It is plausible

327   that rotational and vibrational modes may be excited, seen previously in gas–solid scattering.[82,83]

328   However, we conclude that only rotational degrees of freedom contribute to the extracted values of E_{int}

329   based on the relatively low values of E_i for all four beams and the maximum values of fractional energy

330   loss occurring at $\chi = 90°$. As a result, the lowest lying vibrational modes[84] for CD_4, ND_3, and D_2O, v_4

331   (11.9 kJ mol^{-1}), v_2 (8.95 kJ mol^{-1}), and v_2 (14.1 kJ mol^{-1}), respectively, are unlikely to be populated to a

332   significant degree. It then follows that the differences in internal excitation values between Ne and CD_4,

333   ND_3, and D_2O, 3.2, 3.0, and 3.7 kJ mol^{-1}, respectively, correspond to the rotational energies of the

334   scattered molecules.

335   **IVb. DISCUSSION OF THERMAL DESORPTION FROM DODECANE**

336   The TD fraction derived from the $\theta_i = 60°$ scattering angular distributions, defined as TD/(TD+IS), is

337   plotted in Fig. 7 for Ne, CD_4, ND_3, and D_2O as a function of deflection angle. All four scatterers exhibit

increasing TD fractions as χ increases, except for a slight deviation in the case of Ne scattering at $\chi =$ 30°. It is observed that Ne scattering results in the smallest TD fractions at all values of χ while, for the most part, the polyatomic molecules behave similarly.
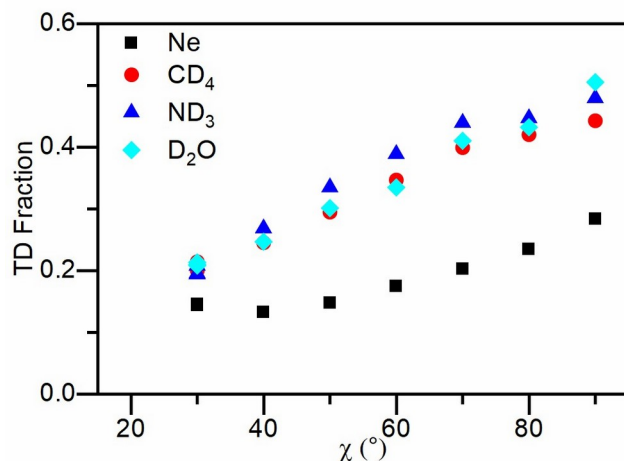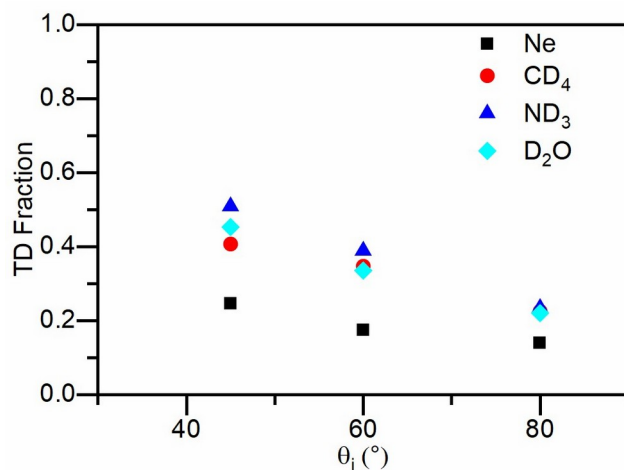

Figure 7. TD fraction as a function of deflection angle for Ne, CD_4, ND_3, and D_2O scattered from a dodecane flat jet at $\theta_i = 60°$.

At a fixed incidence angle, the increasing TD fraction with increasing deflection angle is expected since a larger value of χ corresponds to collisions where more momentum normal to the surface has been lost from the projectile. This trend is also seen for both $\theta_i = 45$ and 80°. Additional factors must be considered to explain why the Ne trend is so different than that of the polyatomic scatterers. For example, the uptake of incidence energy in internal degrees of freedom may correlate with χ or the trapping well depth for Ne may be significantly smaller than for the polyatomic scatterers.

Overall, the observed TD fraction trend of $ND_3 > D_2O \approx CD_4 >$ Ne follows that which has been reported for scattering from squalane at similar beam energies at a single deflection angle $\chi = 90°$.[51] As has been previously pointed out for scattering from squalane, the TD fraction correlates with the projectiles' free energies of solvation $(\Delta G^{\circ}_{solv} = -RT \ln K_H)$.[51] In comparing the TD fraction values for CD_4 (0.40), ND_3 (0.49), and D_2O (0.48) scattered from dodecane with the analogous values for CH_4 (0.49), NH_3 (0.59), and D_2O (0.57) scattered from squalane (interpolated from ref. [51] on the basis of beam energy), we see that scattering from dodecane leads to TD fractions ca. 17% smaller than those for

17

357   squalane scattering. Thus, collisions undergone by these polyatomic scatterers are harder with dodecane,

358   indicating that it is a more rigid surface.

359

360   **Figure 8.** TD fraction at $\theta_f = 60°$ as a function of incidence angle for Ne, CD_4, ND_3, and D_2O scattered
361   from a dodecane flat jet.

362   The dependence of TD fraction on incidence angle is shown in Fig. 8 for the four scatterers. Here, the

363   TD fraction trend of $ND_3 > D_2O \approx CD_4 >$ Ne is seen again. The TD fraction decreases as θ_i increases, as

364   has been seen in other gas–liquid scattering experiments.[35,85,86] Interestingly, this trend is opposite to that

365   observed in single crystal gas–solid scattering experiments.[87-90] Nesbitt[86] has attributed this difference to

366   the increased roughness and corrugation of a liquid surface compared to a single crystal solid surface,

367   leading to the conversion of incident kinetic energy in high θ_i collisions into translational motion away

368   from the liquid surface, and thus the breakdown of normal energy scaling arguments, as the normal

369   energy component scales according to $E_i \cos^2(\theta i)$.

370   **V. EVAPORATION AND SCATTERING FROM COLD SALTY WATER**

371   Initial experiments have been performed on the evaporation and scattering of Ar ($E_i = 41.5$ kJ mol^{-1})

372   from a flat jet of cold salty water, using the instrument shown in Fig. 1. Using a similar strategy to that

373   described above for dodecane, we first characterized the TD channel by observing the evaporation of Ar

374   from an Ar-doped salty water jet. Fig. 9 (a) shows the resultant TOF spectra at $\theta_f = 0, 30,$ and 60°.
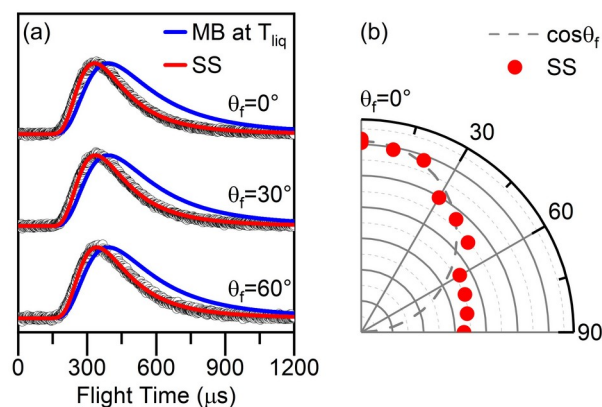
Figure 9. (a) Normalized evaporation TOF spectra of Ar from an Ar-doped aqueous LiBr flat jet at θ_f = 0, 30, and 60°. TOF distributions are fitted by an SS distribution (red traces); an MB distribution (blue traces) at T_{liq} = 226 K is shown for comparison. (b) Angular plot created from the integrated, non-normalized intensities of the SS simulations (red circles) at various detector angles. The cosine function representing the expected angular distribution for evaporation is indicated by the dashed gray curve.

The TOF spectra reflect Ar velocity distributions that are slightly faster than those of a thermal distribution at the temperature of the liquid, shown as a blue trace. This super-Maxwellian character may indicate that Ar–H_2O collisions are occurring in the gas-phase above the surface, accelerating the Ar atoms in a kind of supersonic expansion. However, other explanations are possible. If the sticking probability of Ar is enhanced by incidence translational energy, for example due to a barrier associated with solvent reorganization as has been seen for He/H_2O,[59] detailed balance tells us that evaporating Ar atoms will be emitted with velocities faster than the Boltzmann expectation. For this system, this is unlikely as prior studies have shown that Ar evaporation from cold salty water is Maxwellian.[46] An angular plot of the integrated TOF fits shown in Fig. 9 (b) reveals that evaporation from the jet surface deviates from a $\cos\theta_f$ distribution (dashed gray curve). Given these observations, there likely exists a constant, isotropic background signal emanating from the cryogenically cooled Cu wall in analogy to the dodecane studies.[49,50]

Exploratory measurements were performed on Ar scattering from an aqueous LiBr jet. The resultant TOF spectrum is shown in Fig. 10.
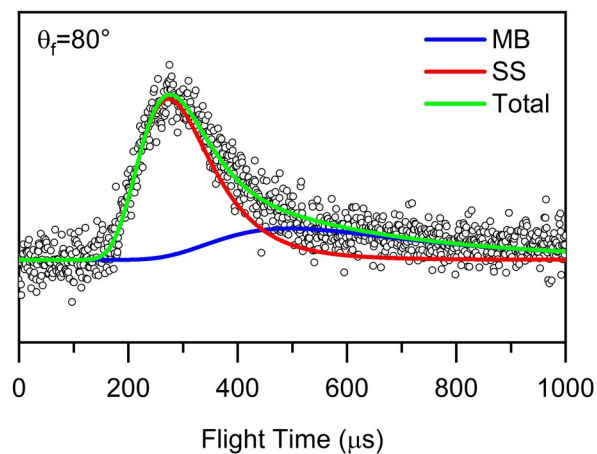
Figure 10. TOF spectrum of Ar scattering from a salty water flat jet with $\theta_i = 60°$ at $\theta_f = 80°$. The data is fitted by the sum of an SS distribution (red trace) and an MB distribution (blue trace) at the liquid jet temperature. The sum of the two contributions is shown by the green trace.

From the integrated fits, a TD fraction of 0.23 is extracted. In comparison to the values measured for particles scattered from dodecane at the same geometry ($\theta_i = 60°$, $\theta_f = 80°$, $\chi = 40°$), this result suggests that Ar has a lower proclivity for impulsive scattering from cold salty water than Ne does from dodecane, but is more prone to IS than CD_4, ND_3, and D_2O from dodecane. While the free energy of solvation successfully describes the trend in TD fraction of the dodecane scatterers, extending this comparison to Ar scattering is nontrivial. To the best of our knowledge, ΔG_{solv}° for Ar in 8 m LiBr has not been measured, and extrapolation from reference data provides only a rough estimate of ca. 39 kJ mol^{-1}, which lies far outside the range of values reported for the dodecane scatterers.[91] Additionally, the mean translational energy of the Ar molecular beam is between 25 and 75% larger than that of the dodecane scattering partners. This results in higher collisional energies and likely plays a role in the relative TD fractions observed for different gas–liquid systems. Further studies are currently underway to characterize and understand the scattering behavior of Ar from a cold salty water jet.

VI. CONCLUSIONS

In this work, we review recent progress in molecular scattering experiments from a volatile flat liquid jet to determine how scatterer and liquid identity affects scattering and energy transfer at the gas–liquid interface. We have reported results on the evaporation of Ne, CD_4, ND_3, and D_2O from doped dodecane

20

415   jets along with the scattering of these four species from pure dodecane jets, as well as evaporation and

416   scattering of Ar from cold salty water jets. The combination of well-defined angular distributions from

417   the flat jet and time-of-flight measurements that characterize the translational energy of the scatterers

418   provides a fundamental understanding of the gas–liquid interface from a mechanistic perspective.

419   The dodecane evaporation TOF profiles for all four species are best described by an MB flux

420   distribution at T_{liq} after background subtraction and exhibit $\cos\theta_f$ angular distributions characteristic of

421   evaporation from a flat surface and a sticking coefficient of unity. In the scattering experiments, the

422   scattering TOF spectra for all four scatterers are fitted by a linear combination of a faster IS component

423   and a slower TD component. Integrating these spectra results in super-specular scattering in the IS

424   channel, attributed to anisotropic momentum transfer at the interface, and $\cos\theta_f$ angular distributions for

425   the TD channel.

426   In the IS channel, the fractional energy loss is smallest for Ne and largest for D_2O. This trend was also

427   found in prior squalane scattering experiments, but the fractional energy loss from dodecane is smaller

428   than from squalane. This shows that squalane is a softer surface than dodecane.

429   The TD fraction is largest for collision trajectories with a larger deflection angle and smallest for

430   grazing trajectories. CD_4, ND_3, and D_2O scattering resulted in similar TD fractions, contrasting with Ne

431   scattering. The relative TD fractions correlate with free energies of solvation in dodecane, consistent

432   with the prior literature. These findings showcase the importance of collision geometry and scatterer

433   identity toward the likelihood of being trapped at the interface. We then applied a soft-sphere kinematic

434   model to describe energy loss in the impulsive mechanistic channel. CD_4, ND_3, and D_2O exhibit larger

435   values for internal excitation than Ne, attributed to rotational excitation of the polyatomic scatterers.

436   The salty water experiments indicated that Ar atoms evaporating from a jet of 8 m LiBr undergo

437   collisions with water vapor above the surface of the jet, resulting in TOF distributions that are slightly

438   super-Maxwellian. Initial results from Ar scattering experiments suggest that Ar is more likely to

439 undergo surface trapping by cold salty water than Ne is on dodecane, but less so than the molecular

440 scatterers from dodecane.

441 We have elucidated interfacial interactions by probing atomic and molecular scattering dynamics at

442 the gas–liquid interface using a flat liquid jet. This work will serve as a useful benchmark for studying

443 future volatile solvent systems including aqueous media. We plan to continue to investigate nonreactive

444 and reactive scattering from a cold salty water flat jet. Preliminary results are presented here, and further

445 experiments are currently underway, supported by the framework established in this body of work.

446

447

448

449

450

451

452

453

454

455

456

457

458

459

460

461

462

463

464

465

AUTHOR INFORMATION

Corresponding Author

Daniel M. Neumark – *Department of Chemistry, University of California, Berkeley, CA 94720, USA*;

Chemical Sciences Division, Lawrence Berkeley National Laboratory, Berkeley, CA 94720, USA;

https://orcid.org/0000-0002-3762-9473; Email: dneumark@berkeley.edu

Authors

Walt Yang – *Department of Chemistry, University of California, Berkeley, CA 94720, USA*; *Chemical*

Sciences Division, Lawrence Berkeley National Laboratory, Berkeley, CA 94720, USA; https://orcid.org/

0000-0003-4296-3801

Madison M. Foreman – *Department of Chemistry, University of California, Berkeley, CA 94720, USA*;

Chemical Sciences Division, Lawrence Berkeley National Laboratory, Berkeley, CA 94720, USA;

https://orcid.org/0000-0002-6516-5426

Steven Saric – *Department of Chemistry, University of California, Berkeley, CA 94720, USA*; *Chemical*

Sciences Division, Lawrence Berkeley National Laboratory, Berkeley, CA 94720, USA; https://orcid.org/

0009-0005-5135-8875

Alec M. Wodtke – *Department of Dynamics at Surfaces, Max Planck Institute for Multidisciplinary*

Sciences, am Faßberg 11, 37077 Göttingen, Germany; *Institute for Physical Chemistry, Georg-August*

University of Göttingen, Tammannstraße 6, 37077 Göttingen, Germany; https://orcid.org/0000-0002-

6509-2183

Kevin R. Wilson – *Chemical Sciences Division, Lawrence Berkeley National Laboratory, Berkeley, CA 94720, USA*; https://orcid.org/0000-0003-0264-0872

Current Addresses

Steven Saric – *Diablo Valley College, Pleasant Hill, CA 94523*

Author Contributions

Walt Yang: Conceptualization (equal); Data curation (lead); Formal analysis (lead); Investigation (lead); Methodology (equal); Software (equal); Writing – original draft (lead); Writing – review & editing (equal).

Madison M. Foreman: Conceptualization (supporting); Data curation (supporting); Formal analysis (supporting); Investigation (supporting); Methodology (supporting); Software (supporting); Writing – original draft (supporting); Writing – review & editing (equal).

Steven Saric: Investigation (supporting); Methodology (supporting); Writing – review & editing (supporting).

Alec M. Wodtke: Investigation (supporting); Methodology (supporting); Project administration (supporting); Supervision (supporting); Validation (supporting); Writing – review & editing (equal).

Kevin R. Wilson: Methodology (supporting); Project administration (supporting); Resources (equal); Supervision (supporting); Validation (supporting); Writing – review & editing (equal).

Daniel M. Neumark: Conceptualization (lead); Methodology (equal); Project administration (lead); Resources (lead); Supervision (lead); Validation (lead); Writing – review & editing (equal).

ACKNOWLEDGMENTS

512 **AUTHOR DECLARATIONS**

513 **Conflict of Interest**

514   The authors declare no conflicts of interest.

515 **DATA AVAILABILITY**

516   The data that support the findings of this study are available from the corresponding author upon

517 reasonable request.

518 **REFERENCES**

519 1.   Uppu RM, Cueto R, Squadrito GL, Pryor WA. What Does Ozone React with at the Air Lung

520 Interface? Model Studies Using Human Red Blood Cell Membranes. *Arch Biochem Biophys*.

521 1995;319(1):257–266.

522 2.   Sosnowski TR, Kubski P, Wojciechowski K. New experimental model of pulmonary surfactant

523 for biophysical studies. *Colloids Surf A*. 2017;519:27-33.

524 3.   Wallington TJ, Kaiser EW, Farrell JT. Automotive fuels and internal combustion engines: a

525 chemical perspective. *Chem Soc Rev*. 2006;35(4):335.

526 4.   Littel R, Van Swaaij WPM, Versteeg GF. Kinetics of carbon dioxide with tertiary amines in

527 aqueous solution. *AIChE J*. 1990;36(11):1633-1640.

528 5.   Dentener FJ, Crutzen PJ. Reaction of N_2O_5 on tropospheric aerosols: Impact on the global

529 distributions of NO $_x$, O_3, and OH. *Journal of Geophysical Research: Atmospheres*. 1993;98(D4):7149-

530 7163.

531   6.   Singh A, Agrawal M. Acid rain and its ecological consequences. *J Environ Biol*. 2008;29:15–24.

532   7.   Donaldson D, Valsaraj KT. Adsorption and reaction of trace gas-phase organic compounds on

533   atmospheric water film surfaces: A critical review. *Environmental science & technology*.

534   2010;44(3):865-873.

535   8.   Putikam R, Lin M-C. A novel mechanism for the isomerization of N_2O_4 and its implication for

536   the reaction with H_2O and acid rain formation. *Int J Quantum Chem*. 2018;118(12):e25560.

537   9.   Ruiz-López MF, Martins-Costa MTC, Anglada JM, Francisco JS. A New Mechanism of Acid

538   Rain Generation from HOSO at the Air–Water Interface. *J Am Chem Soc*. 2019;141(42):16564–16568.

539   10.   Gao X-F, Nathanson GM. Exploring Gas-Liquid Reactions with Microjets: Lessons We Are

540   Learning. *Acc Chem Res*. 2022;55:3294-3302.

541   11.   Nesbitt DJ, Zolot AM, Roscioli JR, Ryazanov M. Nonequilibrium Scattering/Evaporation

542   Dynamics at the Gas-Liquid Interface: Wetted Wheels, Self-Assembled Monolayers, and Liquid

543   Microjets. *Acc Chem Res*. 2023;56:700-711.

544   12.   Devlin SW, Bernal F, Riffe EJ, Wilson KR, Saykally RJ. Spiers Memorial Lecture: Water at

545   interfaces. *Faraday Disc*. 2023;

546   13.   Richmond GL. Molecular Bonding and Interactions at Aqueous Surfaces as Probed by

547   Vibrational Sum Frequency Spectroscopy. *Chem Rev*. 2002;102(8):2693–2724.

548   14.   McGuire JA, Shen YR. Ultrafast Vibrational Dynamics at Water Interfaces. *Science*.

549   2006;313:1945–1948.

550   15.   Petersen PB, Saykally RJ. On the Nature Of Ions at the Liquid Water Surface. *Annu Rev Phys

551   Chem*. 2006;57(1):333–364.

552   16.   Rizzuto AM, Irgen-Gioro S, Eftekhari-Bafrooei A, Saykally RJ. Broadband Deep UV Spectra of

553   Interfacial Aqueous Iodide. *J Phys Chem Lett*. 2016/10/06 2016;7(19):3882-3885.

554   17.   Mizuno H, Rizzuto AM, Saykally RJ. Charge-Transfer-to-Solvent Spectrum of Thiocyanate at

555   the Air/Water Interface Measured by Broadband Deep Ultraviolet Electronic Sum Frequency Generation

556   Spectroscopy. *J Phys Chem Lett*. 2018/08/16 2018;9(16):4753-4757.

557   18.   Bhattacharyya D, Mizuno H, Rizzuto AM, Zhang Y, Saykally RJ, Bradforth SE. New Insights

558   into the Charge-Transfer-to-Solvent Spectrum of Aqueous Iodide: Surface versus Bulk. *J Phys Chem

559   Lett*. 2020;11(5):1656-1661.

560   19.   Mizuno H, Oosterbaan KJ, Menzl G, et al. Revisiting the $\pi \rightarrow \pi^*$ transition of the nitrite ion at the

561   air/water interface: A combined experimental and theoretical study. *Chem Phys Lett*. 2020/07/16/

562   2020;751:137516.

563 20.   Yu C-C, Seki T, Chiang K-Y, et al. Polarization-Dependent Heterodyne-Detected Sum-

564 Frequency Generation Spectroscopy as a Tool to Explore Surface Molecular Orientation and Ångström-

565 Scale Depth Profiling. *J Phys Chem B*. 2022/08/25 2022;126(33):6113-6124.

566 21.   Li Y, Yan X, Cooks RG. The Role of the Interface in Thin Film and Droplet Accelerated

567 Reactions Studied by Competitive Substituent Effects. *Angew Chem Int Ed*. 2016;55(10):3433–3437.

568 22.   Nam I, Lee JK, Nam HG, Zare RN. Abiotic production of sugar phosphates and uridine

569 ribonucleoside in aqueous microdroplets. *PNAS*. 2017;114(47):12396–12400.

570 23.   Diveky ME, Gleichweit MJ, Roy S, Signorell R. Shining New Light on the Kinetics of Water

571 Uptake by Organic Aerosol Particles. *J Phys Chem A*. 2021;125(17):3528–3548.

572 24.   Wokosin KA, Schell EL, Faust JA. Emerging investigator series: surfactants, films, and coatings

573 on atmospheric aerosol particles: a review. *Environmental Science: Atmospheres*. 2022;2(5):775-828.

574 25.   Weinberg WH. Molecular beam scattering from solid surfaces. *Adv Colloid Interface Sci*.

575 1975;4:301–347.

576 26.   Hurst JE, Becker CA, Cowin JP, Janda KC, Wharton L, Auerbach DJ. Observation of Direct

577 Inelastic Scattering in the Presence of Trapping-Desorption Scattering: Xe on Pt(111). *Phys Rev Lett*.

578 1979;43(16):1175–1177.

579 27.   Barker JA, Auerbach DJ. Gas—surface interactions and dynamics; Thermal energy atomic and

580 molecular beam studies. *Surf Sci Rep*. 1984;4(1-2):1-99.

581 28.   Harten U, Lahee AM, Toennies JP, Wöll C. Observation of a Soliton Reconstruction of Au(111)

582 by High-Resolution Helium-Atom Diffraction. *Phys Rev Lett*. 1985;54(24):2619-2622.

583 29.   Huang Y, Rettner CT, Auerbach DJ, Wodtke AM. Vibrational Promotion of Electron Transfer.

584 *Science*. 2000;290(5489):111-114.

585 30.   Faubel M, Schlemmer S, Toennies JP. A molecular beam study of the evaporation of water from

586 a liquid jet. *Z Phys D Atoms, Molecules and Clusters*. 1988;10(2-3):269–277.

587 31.   Faubel M, Kisters T. Non-equilibrium molecular evaporation of carboxylic acid dimers. *Nature*.

588 1989;339(6225):527–529.

589 32.   Ekimova M, Quevedo W, Faubel M, Wernet P, Nibbering ETJ. A liquid flatjet system for

590 solution phase soft-x-ray spectroscopy. *Structural Dynamics*. 2015;2(5):054301.

591 33.   Lednovich SL, Fenn JB. Absolute evaporation rates for some polar and nonpolar liquids. *AIChE

592 Journal*. 1977;23(4):454–459.

593 34.   Siegbahn H. Electron spectroscopy for chemical analysis of liquids and solutions. *J Phys Chem*.

594 1985;89(6):897–909.

595   35.   King ME, Nathanson GM, Hanning-Lee M, Minton TK. Probing the microscopic corrugation of

596   liquid surfaces with gas–liquid collisions. *Phys Rev Lett*. 1993;70(7):1026–1029.

597   36.   Nathanson GM, Davidovits P, Worsnop DR, Kolb CE. Dynamics and Kinetics at the Gas–Liquid

598   Interface. *J Phys Chem*. 1996;100(31):13007–13020.

599   37.   Wu B, Zhang J, Minton TK, et al. Scattering Dynamics of Hyperthermal Oxygen Atoms on Ionic

600   Liquid Surfaces: [emim][NTf$_2$] and [C$_{12}$mim][NTf$_2$]. *J Phys Chem C*. 2010;114(9):4015–4027.

601   38.   Brastad SM, Nathanson GM. Molecular beam studies of HCl dissolution and dissociation in cold

602   salty water. *Phys Chem Chem Phys*. 2011;13(18):8284.

603   39.   Lancaster DK, Johnson AM, Burden DK, Wiens JP, Nathanson GM. Inert Gas Scattering from

604   Liquid Hydrocarbon Microjets. *J Phys Chem Lett*. 2013;4(18):3045–3049.

605   40.   Faust JA, Sobyra TB, Nathanson GM. Gas–Microjet Reactive Scattering: Collisions of HCl and

606   DCl with Cool Salty Water. *J Phys Chem Lett*. 2016;7(4):730–735.

607   41.   Shaloski MA, Gord JR, Staudt S, Quinn SL, Bertram TH, Nathanson GM. Reactions of N$_2$O$_5$

608   with Salty and Surfactant-Coated Glycerol: Interfacial Conversion of Br$^-$ to Br$_2$ Mediated by

609   Alkylammonium Cations. *J Phys Chem A*. 2017;121(19):3708–3719.

610   42.   Sobyra TB, Melvin MP, Nathanson GM. Liquid Microjet Measurements of the Entry of Organic

611   Acids and Bases into Salty Water. *J Phys Chem C*. 2017;121(38):20911–20924.

612   43.   Gord JR, Zhao X, Liu E, Bertram TH, Nathanson GM. Control of Interfacial Cl$_2$ and N$_2$O$_5$

613   Reactivity by a Zwitterionic Phospholipid in Comparison with Ionic and Uncharged Surfactants. *J Phys*

614   *Chem A*. 2018;122(32):6593–6604.

615   44.   Lane PD, Moncrieff KE, Greaves SJ, McKendrick KG, Costen ML. Inelastic Scattering of CN

616   Radicals at the Gas–Liquid Interface Probed by Frequency-Modulated Absorption Spectroscopy. *J Phys*

617   *Chem C*. 2020;124(30):16439–16448.

618   45.   Saecker ME, Govoni ST, Kowalski DV, King ME, Nathanson GM. Molecular Beam Scattering

619   from Liquid Surfaces. *Science*. 1991;252:1421–1424.

620   46.   Faust JA, Nathanson GM. Microjets and coated wheels: versatile tools for exploring collisions

621   and reactions at gas–liquid interfaces. *Chem Soc Rev*. 2016;45(13):3609–3620.

622   47.   Koralek JD, Kim JB, Brůža P, et al. Generation and characterization of ultrathin free-flowing

623   liquid sheets. *Nat Commun*. 2018;9(1)

624   48.   Lee C, Pohl MN, Ramphal IA, et al. Evaporation and Molecular Beam Scattering from a Flat

625   Liquid Jet. *J Phys Chem A*. 2022;126(21):3373–3383.

626   49.   Yang W, Lee C, Saric S, Pohl MN, Neumark DM. Evaporation and scattering of neon, methane,

627   and water from a dodecane flat liquid jet. *J Chem Phys*. 2023;159(5)

628   50.   Saric S, Yang W, Neumark DM. Molecular beam scattering of ammonia from a dodecane flat

629   liquid jet. *Faraday Disc*. 2024;Advance Article

630   51.   Saecker ME, Nathanson GM. Collisions of protic and aprotic gases with hydrogen bonding and

631   hydrocarbon liquids. *J Chem Phys*. 1993;99(9):7056–7075.

632   52.   Kinefuchi I, Yamaguchi H, Shiozaki S, Sakiyama Y, Matsumoto Y. Out-of-plane Scattering

633   Distribution of Nitrogen Molecular Beam on Graphite (0001) Surface. *AIP Conf Proc*. 2005;762(947)

634   53.   Tesa-Serrate MA, Smoll EJ, Minton TK, McKendrick KG. Atomic and Molecular Collisions at

635   Liquid Surfaces. *Annu Rev Phys Chem*. 2016;67(1):515–540.

636   54.   Sobyra TB, Pliszka H, Bertram TH, Nathanson GM. Production of Br_2 from N_2O_5 and Br^- in

637   Salty and Surfactant-Coated Water Microjets. *J Phys Chem A*. 2019/10/17 2019;123(41):8942-8953.

638   55.   Lee YT, McDonald JD, Lebreton PR, Herschbach DR. Molecular Beam Reactive Scattering

639   Apparatus with Electron Bombardment Detector. *Rev Sci Instrum*. 1969;40(11):1402–1408.

640   56.   Lee YT. Molecular Beam Studies of Elementary Chemical Processes (Nobel Lecture). *Angew*

641   *Chem Int Ed Engl*. 1987;26(10):939–951.

642   57.   Irimia D, Dobrikov D, Kortekaas R, et al. A short pulse (7 μs FWHM) and high repetition rate

643   (dc-5kHz) cantilever piezovalve for pulsed atomic and molecular beams. *Rev Sci Instrum*.

644   2009;80(11):113303.

645   58.   Meng C, Janssen MHM. Measurement of the density profile of pure and seeded molecular beams

646   by femtosecond ion imaging. *Rev Sci Instrum*. 2015;86(2):023110.

647   59.   Hahn C, Kann ZR, Faust JA, Skinner J, Nathanson GM. Super-Maxwellian helium evaporation

648   from pure and salty water. *J Chem Phys*. 2016;144(4)

649   60.   Sasse K, Jose J, Merlin JC. A static apparatus for measurement of low vapor pressures.

650   Experiment results on high molecular-weight hydrocarbons. *Fluid Phase Equilib*. 1988;42:287–304.

651   61.   Lemmon EW, Huber ML. Thermodynamic Properties of *n*-Dodecane. *Energy Fuels*.

652   2004;18(4):960–967.

653   62.   Comsa G, David R. Dynamical parameters of desorbing molecules. *Surf Sci Rep*. 1985;5:145–

654   198.

655   63.   Day C. In: Brandt D, ed. *CAS—CERN Accelerator School: Vacuum in Accelerators*. CERN;

656   2007:241–274.

657 64.   Brenig W. Dynamics and kinetics of gas-surface interaction: Sticking, desorption and inelastic

658 scattering. *Phys Scr*. 1987;35(3):329.

659 65.   Kennard EH. *Kinetic Theory of Gases*. McGraw-Hill Book Company; 1938.

660 66.   Kann ZR, Skinner JL. Sub- and super-Maxwellian evaporation of simple gases from liquid

661 water. *J Chem Phys*. 2016;144(15):154701.

662 67.   Morse MD. In: Dunning FB, Hulet RG, eds. *Atomic, Molecular, and Optical Physics: Atoms and*

663 *Molecules*. Academic Press; 1996:21–47.

664 68.   Lebehot A, Kurzyna J, Lago V, Dudeck M, Campargue R. In: Campargue R, ed. *Atomic and*

665 *Molecular Beams*. Springer; 2001:237–251.

666 69.   Kinefuchi I, Kotsubo Y, Osuka K, et al. Incident energy dependence of the scattering dynamics

667 of water molecules on silicon and graphite surfaces: the effect on tangential momentum accommodation.

668 *Microfluidics and Nanofluidics*. 2017;21(2)

669 70.   Subbarao RB, Miller DR. Velocity distribution measurements of 0.06–1.4 eV argon and neon

670 atoms scattered from the (111) plane of a silver crystal. *J Chem Phys*. 1973;58(12):5247-5257.

671 71.   Rettner CT, Delouise LA, Auerbach DJ. Effect of incidence kinetic energy and surface coverage

672 on the dissociative chemisorption of oxygen on W(110). *J Chem Phys*. 1986;85(2):1131-1149.

673 72.   Alexander WA, Zhang J, Murray VJ, Nathanson GM, Minton TK. Kinematics and dynamics of

674 atomic-beam scattering on liquid and self-assembled monolayer surfaces. *Faraday Disc*. 2012;157:355.

675 73.   Andric N, Jenny P. Molecular dynamics investigation of energy transfer during gas-surface

676 collisions. *Phys Fluids*. 2018;30(7):077104.

677 74.   Rettner CT, Ashfold MNR. *Dynamics of Gas-Surface Interactions*. Royal Society of Chemistry;

678 1991.

679 75.   Nathanson GM. Molecular Beam Studies of Gas–Liquid Interfaces. *Annu Rev Phys Chem*.

680 2004;55(1):231–255.

681 76.   Saecker ME, Nathanson GM. Collisions of protic and aprotic gases with hydrogen bonding and

682 hydrocarbon liquids. *The Journal of Chemical Physics*. 1993;99:7056–7075.

683 77.   Williams MA, Koehler SP. MD simulations of He evaporating from dodecane. *Chem Phys Lett*.

684 2015;629:53-57.

685 78.   Lorentz HA. Ueber die Anwendung des Satzes vom Virial in der kinetischen Theorie der Gase.

686 *Annalen der Physik*. 1881;248(1):127–136.

687 79.   Berthelot D. Sur le mélange des gaz. *Comptes rendus hebdomadaires des séances de l'Académie*

688 *des Sciences*. 1898;126:1703–1855.

689   80.   Mourits FM, Rummens FHA. A critical evaluation of Lennard-Jones and Stockmayer potential

690   parameters and of some correlation methods. *Can J Chem*. 1977;55(16):3007–3020.

691   81.   Chen C-K, Banaszak M, Radosz M. Statistical Associating Fluid Theory Equation of State with

692   Lennard-Jones Reference Applied to Pure and Binary *n*-Alkane Systems. *J Phys Chem B*.

693   1998;102(13):2427–2431.

694   82.   Rettner C, Fabre F, Kimman J, Auerbach D. Observation of direct vibrational excitation in gas-

695   surface collisions: NO on Ag (111). *Phys Rev Lett*. 1985;55(18):1904.

696   83.   Kay BD, Raymond T, Coltrin ME. Observation of Direct Multiquantum Vibrational Excitation

697   in Gas-Surface Scattering: NH_3 on Au (111). *Phys Rev Lett*. 1987;59(24):2792.

698   84.   Shimanouchi T. *Tables of molecular vibrational frequencies*. vol 1. National Bureau of

699   Standards Washington, DC; 1972.

700   85.   King ME, Fiehrer KM, Nathanson GM, Minton TK. Effects of Thermal Roughening on the

701   Angular Distributions of Trapping and Scattering in Gas–Liquid Collisions. *J Phys Chem A*.

702   1997;101(36):6556-6561.

703   86.   Perkins BG, Nesbitt DJ. Toward Three-Dimensional Quantum State-Resolved Collision

704   Dynamics at the Gas–Liquid Interface: Theoretical Investigation of Incident Angle. *J Phys Chem A*.

705   2009;113(16):4613-4625.

706   87.   Mullins CB, Rettner CT, Auerbach DJ, Weinberg WH. Variation of the trapping probability of

707   Ar on Pt(111) with kinetic energy and angle of incidence: The changing role of parallel momentum with

708   surface temperature. *Chem Phys Lett*. 1989;163(2–3):111-115.

709   88.   Rettner CT, Mullins CB, Bethune DS, Auerbach DJ, Schweizer EK, Weinberg WH. Molecular

710   beam studies of trapping dynamics. *J Vac Sci Technol A*. 1990;8:2699-2704.

711   89.   Head-Gordon M, Tully JC, Rettner CT, Mullins CB, Auerbach DJ. On the nature of trapping and

712   desorption at high surface temperatures. Theory and experiments for the Ar–Pt(111) system. *J Chem

713   Phys*. 1991;94(2):1516–1527.

714   90.   Rettner CT, Kimman J, Auerbach DJ. Inelastic scattering of NO from Ag(111): Internal state,

715   angle, and velocity resolved measurements. *J Chem Phys*. 1991;94:734-750.

716   91.   Hamme RC, Emerson SR. The solubility of neon, nitrogen and argon in distilled water and

717   seawater. *Deep Sea Research Part I: Oceanographic Research Papers*. 2004;51(11):1517-1528.

718
719
720
721

722
723
724
725
726
727
728
729
730
731
732
733
734
735
736
737
738
739
740
741
742
743
744
745
746
747
748 **Table 1.** Average fractional energy loss in the IS Channel at a deflection angle of $\chi = 90°$ and soft-
749 sphere fitted parameters for all values of χ.

Scattered Species	Fractional Energy Loss $\Delta E / E_i$		Soft-Sphere Fitted Parameters	
	Dodecane	[a]Squalane	Effective Surface Mass m_{eff} (amu)	Total Internal Excitation $E_{\int ιι}$ (kJ mol^{-1})
Ne	0.46	0.42	61	2.1
CD$_4$	0.61	[b]0.49	52	5.3
ND$_3$	0.62	[c]0.52	55	5.1
D$_2$O	0.64	0.56	54	5.8

750 [a]Gas scattering from liquid squalane. Values interpolated from Fig. 4 in ref. [51] to directly compare
751 scattering at identical beam energies for each species. [b]Value reported for CH$_4$. [c]Value reported for NH$_3$.